ARTICLE   OPEN

Check for updates

Atmospheric modes fiddling the simulated ENSO impact on tropical cyclone genesis over the Northwest Pacific

Jiuwei Zhao [ID][1], Ruifen Zhan [ID][2][✉], Hiroyuki Murakami [ID][3], Yuqing Wang [ID][4][✉], Shang-Ping Xie [ID][5], Leying Zhang[6] and Yipeng Guo [ID][7]

The El Niño-Southern Oscillation (ENSO) is crucial to the interannual variability of tropical cyclone (TC) genesis over the western North Pacific (WNP). However, most state-of-the-art climate models exhibit a consistent pattern of uncertainty in the simulated TC genesis frequency (TCGF) over the WNP in ENSO phases. Here, we analyze large ensemble simulations of TC-resolved climate models to identify the source of this uncertainty. Results show that large uncertainty appears in the South China Sea and east of the Philippines, primarily arising from two distinct atmospheric modes: the Matsuno-Gill-mode (MG-mode) and the Pacific-Japan-like pattern (PJ-mode). These two modes are closely associated with anomalous diabatic heating linked to tropical precipitation bias in model simulations. By conditionally constraining either of the modes, we can significantly reduce model uncertainty in simulating the dipole structure of the TCGF anomalies, confirming that it is the atmospheric circulation bias in response to tropical precipitation bias that causes uncertainty in the simulated WNP TCGF.

INTRODUCTION

Tropical cyclones (TCs) that form over the western North Pacific (WNP) constitute approximately one-third of global annual TC genesis frequency (TCGF)[1], and are known to have a tremendous impact on the coastal countries of Southeast and East Asia. Identifying factors that affect TC variability on various timescales is essential to improving the simulation and prediction skills, and thus minimizing loss of life and property[2,3].

The El Niño-Southern Oscillation (ENSO)[4], a dominant tropical climate mode[5], plays a crucial role in regulating the interannual variability of TC activities worldwide, including their intensity[6], genesis locations, and dominant tracks[5,7,8]. Over the WNP, during the developing phase of El Niño, TCGF tends to increase over the southeastern quadrant of the WNP (SE_WNP) but decrease over the northwestern quadrant of the WNP (NW_WNP), causing a see-saw variation in TCGF over the WNP[5]. Conversely, in La Niña events, more TCs form over the NW_WNP, facilitating landfall and posing a greater risk to coastal populations in Southeast Asia. The capability of climate models to accurately simulate this see-saw structure is crucial for predicting and projecting future changes in TCGF[9,10]. However, few studies have focused on or discussed the uncertainty of TCGF simulations during the warm and cold ENSO phases in a specific region[8,11].

Numerous previous studies have indicated that uncertainty of climate simulations mainly comes from scenario uncertainty, model uncertainty, and internal variability[9,10,12,13]. Scenario uncertainty results from the different radiative forcing[12,14,15], which can cause changes in the mean state (e.g., El Niño- or La Niña-like SST warming pattern) and consequently influence the TCGF[16–21]. Model uncertainty arises from the model dynamical core, physics, and resolution that affect the internal variability

intrinsic to the climate system[13]. The internal uncertainty stems from internal natural variabilities, such as interdecadal Pacific Oscillation[14,22–24] and Atlantic Multidecadal Oscillation[25,26]. These internal variabilities are treated as the ocean dynamical processes and often believed to be the origins of uncertainty in climate simulations. In coupled ocean-atmospheric models, uncertainties may originate from both oceanic and atmospheric processes, which is hard to be considered separately. Our recent study[11] has shown that large biases exist in the simulated TCGF over the western part of the WNP in most climate models. Both interannual and interdecadal variabilities could not be reasonably captured even the atmospheric models are forced by observational SSTs, indicating that the uncertainty could result from the internal atmospheric processes. However, the uncertainty caused by the internal atmospheric processes on interannual timescale has not been identified or quantified. This becomes a barrier to improving the reliability of both seasonal prediction and climate projection of TC activities in the WNP by climate models.

In this study, we first evaluate the atmosphere-induced uncertainty of the simulated TCGF over the WNP in response to ENSO by state-of-the-art climate models forced by observed SST. We then identify the distinct atmospheric modes that are responsible for this uncertainty by conducting regression analysis using a large number of ensemble simulations. We further present results from ensemble simulations by constraining the identified key atmospheric modes responsible for the uncertainty to confirm that it is the atmospheric modes that contribute to the uncertainty of the simulated TCGF over the WNP in response to ENSO events. Finally, we explore the origin of the atmospheric modes contributing to the uncertainty in model simulations.

[1]Collaborative Innovation Center on Forecast and Evaluation of Meteorological Disasters (CIC-FEMD), Institute of Climate and Application Research (ICAR), Nanjing University of Information Science & Technology (NUIST), Nanjing, China. [2]Department of Atmospheric and Oceanic Sciences/Institute of Atmospheric Sciences, Fudan University, Shanghai, China. [3]Geophysical Fluid Dynamical Laboratory, Princeton University, Princeton, NJ, USA. [4]Department of Atmospheric Sciences and International Pacific Research Center (IPRC), University of Hawaii at Manoa, Honolulu, HI, USA. [5]Scripps Institution of Oceanography, University of California San Diego, La Jolla, CA, USA. [6]College of Biology and Environment, Joint Innovation Center for Modern Forestry Studies, Nanjing Forestry University, Nanjing, China. [7]School of Atmospheric Sciences, Nanjing University, Nanjing, China. ✉email: zhanrf@fudan.edu.cn; yuqing@hawaii.edu
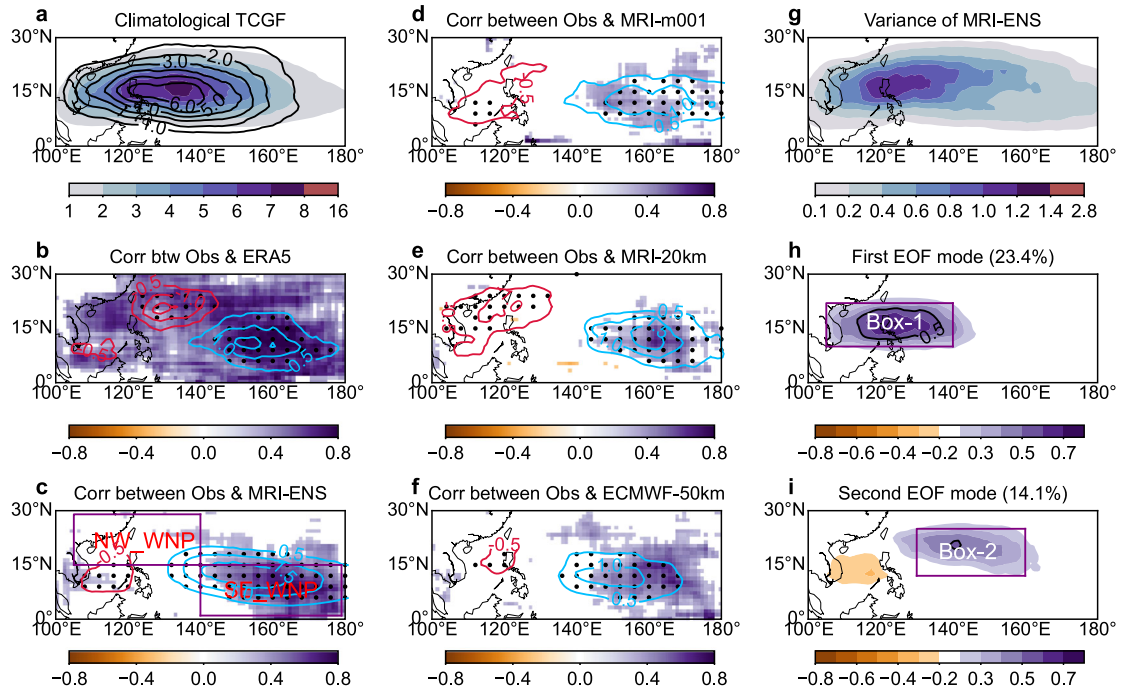
Fig. 1 Uncertainty in the simulated TCGF over the WNP. a Observed (black contours) and MRI-AGCM ensemble mean (shaded) JJASON TCGFs averaged from 1951 to 2010; **b** correlation coefficients (shaded) between the observed and ERA5 TCGFs over each grid box for 1951–2010 period, and the composite difference in the observed TCGF (contours) between 12 El Niño and 12 La Niña events; **c** same as (**b**) but for correlation between the observed and ensemble mean TCGFs (shaded), and composite difference in ensemble mean of 100 members (contours); **d**–**f** same as (**c**) but for TCGF (**d**) only from one MRI member (member-1), **e** from the 20-km MRI run, **f** from 5-member averaged ECMWF runs; **g** the standard deviation calculated from the spreads of TCGF differences between the warm and cold ENSO events across 100 ensemble members relative to ensemble mean (shaded); **h** the first EOF mode of TCGF differences between the warm and cold ENSO events with the 100 members treated as the time dimension; and **i** as in (**h**) but for the second EOF mode. The shades (dots) represent area above 90% confidence level based on two-tailed Student's *t* test in (**b**–**f**) for correlation (composite) map; the purple boxes in (**c**) represent respective NW_WNP (15°N–30°N, 105°E–140°E) and SE_WNP (EQ-15°N, 140°E–180°) regions; in (**h**) the purple box marked with "Box-1" represents the dominant region of TCGF simulation uncertainty (10°N–22°N, 105°E–140°E) while the "Box-2" in (**i**) represents the second region of simulation uncertainty (12°N–25°N, 130°E–160°E).

RESULTS

Uncertainty in the simulated TCGF over the WNP

We first compare in Fig. 1a the climatological mean TCGFs between the multi-member ensemble mean from the Meteorological Research Institute (MRI) of Japan and observations averaged from June to November (JJASON) during 1951–2010. Note that we selected the MRI model because it contains very large ensemble members with permitted resolutions to derive the intermember uncertainty while other models have either the limited ensemble members or relatively coarse resolutions. The spatial distributions in both the observed and simulated TCGFs display high consistency, with high TCGFs centered east of the Philippines (Fig. 1a), suggesting that the state-of-the-art climate models can proficiently simulate the climatological distribution of TCGF over the WNP. The difference in the observed TCGF between El Niño and La Niña events shows a dipole pattern (Fig. 1b, contours) with an increase in TCGF over the SE_WNP and a decrease over the NW_WNP[5,27–29]. The TCGF extracted from the fifth generation of high-resolution reanalysis data from the European Center of Medium-Range Weather Forecasts (ERA5) captures the observed TCGF variability with significant positive correlations in the whole WNP basin (Fig. 1b, shades). However, the correlation between the ensemble mean TCGF and the observed TCGF is only high over the SE_WNP, while that over the other regions is weak and insignificant (Fig. 1c, shades), implying large simulation uncertainty over the NW_WNP. Similar uncertainty appears in the difference in the simulated TCGF between El Niño and La Niña events (Fig. 1c, contours). Since all MRI model runs are forced by observed SST and sea ice, which means that the

uncertainty contributed by oceanic internal variability and air-sea interaction processes is suppressed, the uncertainty should result from the atmospheric processes.

As ENSO has a significant impact on TCGF over the SE_WNP and NW_WNP (Fig. 1b, contours)[5], we evaluate the skills of the 100-member simulations in reproducing the TCGFs averaged in the two sub-regions during 1951–2010. The temporal correlation between the observed and ensemble mean TCGF over the entire WNP is insignificant ($r = 0.2$) (Supplementary Fig. 1a), with correlation coefficients between observations and individual simulations ranging from negative to positive (Supplementary Fig. 1b), indicating that large uncertainty exists in the simulations. Interestingly, we find that over the SE_WNP the ensemble mean TCGF differences are highly correlated with the observed, with a correlation coefficient of 0.66 during 1951–2010 (Supplementary Fig. 1c). The box-and-whisker plot shows that such significant correlation occurs in all members (Supplementary Fig. 1d), indicating that the interannual variability of TCGF over the SE_WNP in response to ENSO can be well captured by the model. However, over the NW_WNP, most members fail to capture the variability of the observed TCGF (Fig. 1c and Supplementary Fig. 1e, f), suggesting large model uncertainty for the region. We further evaluate the signal-to-noise ratio (SNR, Eq. (1) in "Methods") among the 100 members, where larger SNR values indicate higher simulation skills and greater predictability. The SNR over the NW_WNP is lower than that over the SE_WNP (Supplementary Fig. 2c, f). The former largely contributes to low SNR for the whole WNP TCGF. Note that the ensemble mean can significantly improve the simulation skills and reduce the
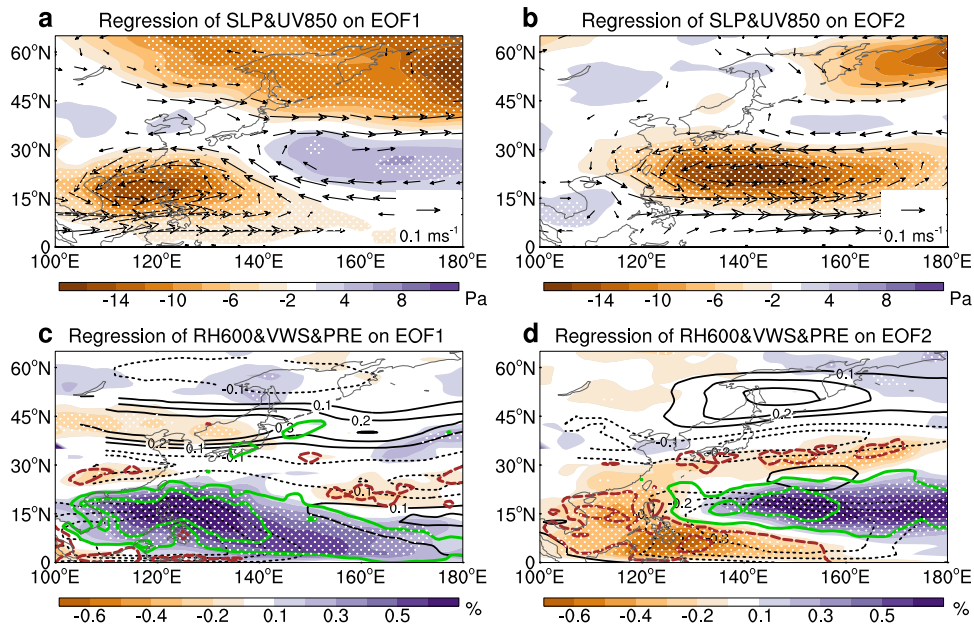
Fig. 2 Two atmospheric modes responsible for the uncertainty in the simulated WNP TCGF response to ENSO. a Regressed SLP (unit: Pa; shaded) and winds at 850 hPa (unit: m s^{-1}; vector) upon the first principal component (PC1; treating 100 members as the time series) derived from the EOF analysis of TCGF differences between the warm and cold ENSO events; **b** regressed SLP and 850-hPa winds upon the second principal component (PC2); **c, d** regressed relative humidity (RH; %, shaded) at 600-hPa, vertical wind shear between 200 and 850 hPa (unit: m s^{-1}, dashed black contours) and precipitation (unit: mm, green and brown contours) upon **c** PC1 and **d** PC2. The shades and vectors represent areas significant above 90% confidence level based on two-sided Student's t test.

simulation uncertainty, in sharp contrast to the individual member (e.g., member-1) as depicted in Fig. 1d.

Previous studies have pointed out that the TCGF simulation skills can be improved with increasing model resolution[30,31]. We also notice that the correlation coefficients of the TCGF in the high-resolution (~20 km, Fig. 1e) simulations with the observed are higher than those in the corresponding low-resolution (~60 km, Fig. 1d) simulations over the SE_WNP, indicating the better simulation skill for the SE_WNP TCGF with the finer resolution. However, over the NW_WNP, simulations using both the high- and low-resolution MRI models exhibit similar low correlations, indicating that the uncertainty in simulated TCGF over the NW_WNP in response to ENSO is not strictly resolution-dependent[9]. Note that this uncertainty is not confined to the MRI model because similar spatial distributions of correlations are also found in ECMWF model (Fig. 1f) and many other models from the Coupled Model Intercomparison Project Phase 6 (CMIP6; Supplementary Fig. 2 in our previous study[11]). As a result, it is deemed to be robust that there exists large uncertainty in the simulated TCGF over the NW_WNP in response to ENSO, where TCs are more likely to make landfall and pose a greater risk to coastal populations in East Asia. It also ultimately lowers the confidence in seasonal prediction and future climate projection of TCGFs for the region by current climate models.

To quantify the uncertainty, we first examine the standard deviation calculated from the spreads (anomalies) based on the composite of TCGF differences between the warm and cold ENSO events across 100 ensembles relative to the ensemble mean (Fig. 1g). Although the TCGF response to ENSO shows a dipole pattern (Fig. 1b, c), the spread shows a similar pattern to the climatological mean TCGF (Fig. 1g, a), with the maximum centered east of the Philippines. We then conduct an empirical orthogonal function (EOF) analysis of the spreads using the 100 samples of TCGF differences between the warm and cold ENSO events as the time series (Fig. 1h, i). The first EOF mode demonstrates large uncertainty in the simulated TCGF differences from the northern part of the South China Sea (SCS) to the east of the Philippines,

namely the Box-1 region (Fig. 1h; 10°N–22°N, 105°E–140°E), consistent with the maximum center of the climatological mean TCGF (Fig. 1a). The second EOF mode shows a positive region centered over the central WNP (12°N–25°N, 130°E–160°E), namely the Box-2 region, accompanied with a weak negative region centered over the SCS. These two modes are statistically significant above 90% confidence level based on the North test[32] and collectively explain 37.5% of the variance of the simulated TCGF difference in response to the warm and cold ENSO events, with the first (second) mode explaining 23.4% (14.1%) of the total variance. Note that the uncertainty in the response of the simulated TCGF over the NW_WNP appears in both the Box-1 and Box-2 regions.

Atmospheric modes responsible for the uncertainty

A question arises as to what physical processes are responsible for the uncertainty. To address this issue, we regress 100 slices of circulation differences between the warm and cold ENSO events upon the two respective principal components (PCs, Fig. 2). Figure 2a shows a strong anomalous cyclonic circulation in the region (0°–30°N, 100°E–140°E) accompanied with easterly wind anomalies over the SE_WNP when regressing 850-hPa winds upon the first PC (PC1). This pattern with a closed cyclonic circulation could represent the simulation bias of the monsoon trough. The westerly-easterly winds compose a typical horizontal shear, which benefits for TC genesis in the monsoon trough. Therefore, a cyclonic or anticyclonic circulation anomaly is associated with a stronger or weaker monsoon trough. The monsoon trough is theoretically related to the off-equatorial Matsuno-Gill mode (MG-mode)[33,34] with the cyclonic gyre circulation resembling the Rossby wave response to diabatic heating north of the equator (Fig. 2a). The regressed winds and sea level pressure upon the second PC (PC2) show a sandwich structure with two large anomalous cyclonic circulations, respectively, in the tropics and high latitudes, and an anomalous anticyclonic circulation in between (Fig. 2b). This circulation pattern is similar to that of the Pacific-Japan mode (PJ-mode)[35,36] or the East Asian Pacific

pattern (EAP)[37]. Both the MG-mode and PJ-mode show a coherent precipitation pattern (Fig. 2c, d), suggesting that these two atmospheric modes could be triggered by tropical convection[33–35,37]. The basin-uniform precipitation (Fig. 2c, green and brown contours) corresponds to the MG-mode, while the dipole precipitation pattern (Fig. 2d, green and brown contours) corresponds to the PJ-mode.

The above two atmospheric modes responsible for the uncertainty in the simulated ENSO-TCGF relationship are derived from 100-member atmospheric circulation differences between the warm and cold ENSO events. We further extract these two modes from the 60-year data of the 100 members (see "Methods") and find that the MG-mode exists in the second EOF mode of most ensemble members (Supplementary Fig. 3a). The spatial correlations of the observed regressed patterns (Fig. 2a) obtained from EOF analysis of 850-hPa winds are significantly high (Supplementary Fig. 3b), consistent with the modes derived from 60-year data for each member (Supplementary Fig. 3c). Also, the PJ-mode derived from 850-hPa vorticity is robust in each of the ensemble members (Supplementary Fig. 3d, f).

The two atmospheric modes have a large impact on WNP TCGF, which largely modulate the simulated ENSO-TCGF relationship and control the simulation uncertainty (Fig. 3). Figure 3a shows the scatter plot of ENSO and NW_WNP TCGF for both observation (black line) and simulations (blue dots and red line). The observed TCGF over the NW_WNP exhibits a significant negative correlation with ENSO ($r = -0.48$), while the correlation in the ensemble mean is insignificant ($r = 0.1$). Moreover, the correlations between ENSO and the simulated TCGF over the NW_WNP for all individual members are diverse and weak, with the correlation coefficients ranging from -0.2 to 0 between 25% and 75% percentiles for 100 ensemble members. This confirms that the simulated TCGF response to ENSO over the NW_WNP has large uncertainty. However, over the SE_WNP, the correlations between ENSO and the simulated (observed) TCGF in all individual members are significantly positive ($r = 0.86$), implying high confidence in the model simulated TCGF over the SE_WNP (Fig. 3b). The correlation between ENSO and the observed TCGF over the whole WNP is insignificant ($r = 0.06$) but that between ENSO and the simulated WNP TCGF is significant (Fig. 3c). The MG-mode has a significant correlation with ENSO in both simulations and observation (Fig. 3d). It has a strong impact on the simulated TCGF in Box-1 with the correlation coefficient reaching 0.76, while the correlation between the MG-mode and Box-1 TCGF in observation is much weaker ($r = 0.23$; Fig. 3e). Although the TCGF in Box-1 has a significant correlation with the MG-mode in simulations ($r = 0.57$) during ENSO years (Fig. 3f), the MG-mode indices show large variations ranging from positive to negative (-0.65 to 0.15) during both El Niño and La Niña years (Fig. 3d). As a result, the ensemble mean TCGFs in the warm and cold ENSO events have little difference, leading to large uncertainty of TCGF simulations (Fig. 3f; large spread of bars covering both positive and negative ENSO phases). The PJ-mode exhibits a high correlation ($r = 0.81$) with the ENSO index during 1951–2010 in observation, while the correlation in simulations is relatively weak but still statistically significant ($r = 0.44$; Fig. 3g). Interestingly, the PJ-mode has a strong impact on the simulated TCGF in Box-2 ($r = 0.92$), while the correlation in observation is relatively weak ($r = 0.54$; Fig. 3h) but still significant. Generally, a large portion of the PJ-modes among the 100 members are positive during El Niño events and negative during La Niña years, leading to a significant correlation between Box-2 TCGF and PJ-modes between the warm and cold ENSO events ($r = 0.94$).

Improving TCGF simulations in response to ENSO by constraining atmospheric modes

Since the two atmospheric modes are responsible for the uncertainty in the simulated ENSO impact on TCGF over the WNP, TCGF simulations, especially the dipole pattern of TCGF anomalies (Fig. 1b vs Fig. 1c), could be improved by constraining the two modes. First, we explore the TCGF difference between the positive and negative MG and PJ phases (Fig. 4a, b). Further considering the TCGF anomalies during respective warm and cold ENSO events by sorting the 100 MG-mode (PJ-mode) indices (Fig. 4c–f). The selective sampling from the simulations with the bottom 25% negative MG-mode cases, corresponding to an anomalous anticyclonic circulation, in El Niño years (Fig. 4c) shows a dipole pattern over the WNP, which is significantly enhanced compared to the ensemble mean (Fig. 1c) and becomes comparable to the observed pattern (Fig. 1b). This demonstrates that under the control of strong anticyclone over the WNP associated with the MG-mode, convective activities and TC genesis are suppressed in the NW_WNP. As a result, the simulations of the El Niño impact on TCGF over the NW_WNP is greatly improved. Similar improvement in the simulations with the top 25% positive MG-mode cases, corresponding to an anomalous cyclonic circulation, can be found in La Niña years (Fig. 4e). Second, we examined the TCGF anomaly by comparing the bottom (weak positive PJ phase) and the top (strong positive PJ phase) 25% percentiles of the PJ-modes (Fig. 4b) because the PJ-mode is quite strong during the warm ENSO phase in simulations. Results show that the Northwest-Southeast-oriented dipole pattern of the ENSO impact on TCGF is better captured in the simulations with the bottom (top) 25% PJ cases selected only in El Niño (La Niña) years (Fig. 4d, f).

We also explore the probability density function (PDF) distribution of the simulated TCGFs from the 100 members in response to ENSO in Box-1 and Box-2, respectively (Fig. 5). Prior to constraint of the MG-mode, the TCGF in Box-1 shows little difference between El Niño and La Niña events (Fig. 5a, c, gray curves). However, the TCGF in Box-1 saliently decreased (yellow; bottom 25% percentile) during El Niño years and increased (yellow; top 25% percentile) during La Niña years after constraint of the MG-mode (Fig. 5a, c). Although the TCGF in Box-2 is different between El Niño and La Niña events, the magnitudes are largely modulated after the PJ-mode is constrained (Fig. 5b, d), which leads to a more realistic dipole pattern of TCGF response as in observations (Figs. 5d, f and 1b). The results with the MG-mode and the PJ-mode constrained further demonstrate that it is the atmospheric circulation (bias) modes that cause the uncertainty in the simulated WNP TCGF. Therefore, the TCGF prediction and projection of the dipole structure of WNP TCGF anomalies during the warm and cold ENSO phases could be improved by conditionally constraining the corresponding atmospheric modes from large ensemble simulations.

Origin of the two atmospheric modes of the uncertainty

Previous modeling[38–40] and theoretical[33–35,37] studies have demonstrated that the precipitation anomaly with the mean state of high moisture over the WNP warm pool can trigger the convectively-forced coupled Rossby–Kelvin wave or the MG-type response (Fig. 2a), and with the background southerly winds in summer, the convective forcing can trigger the PJ mode or the EAP teleconnection pattern (Fig. 2b). We further deepen the understanding that, due to the baroclinic response to diabatic heating in the tropics, the response in wind anomalies to anomalous precipitation is opposite in the lower and upper troposphere, which is reflected in the response of the vertical shear of zonal wind (Supplementary Fig. 4). To reveal the origin of the identified two atmospheric modes, we conduct the EOF analysis of precipitation differences between the warm and cold ENSO events from the 100 ensemble members. The results show
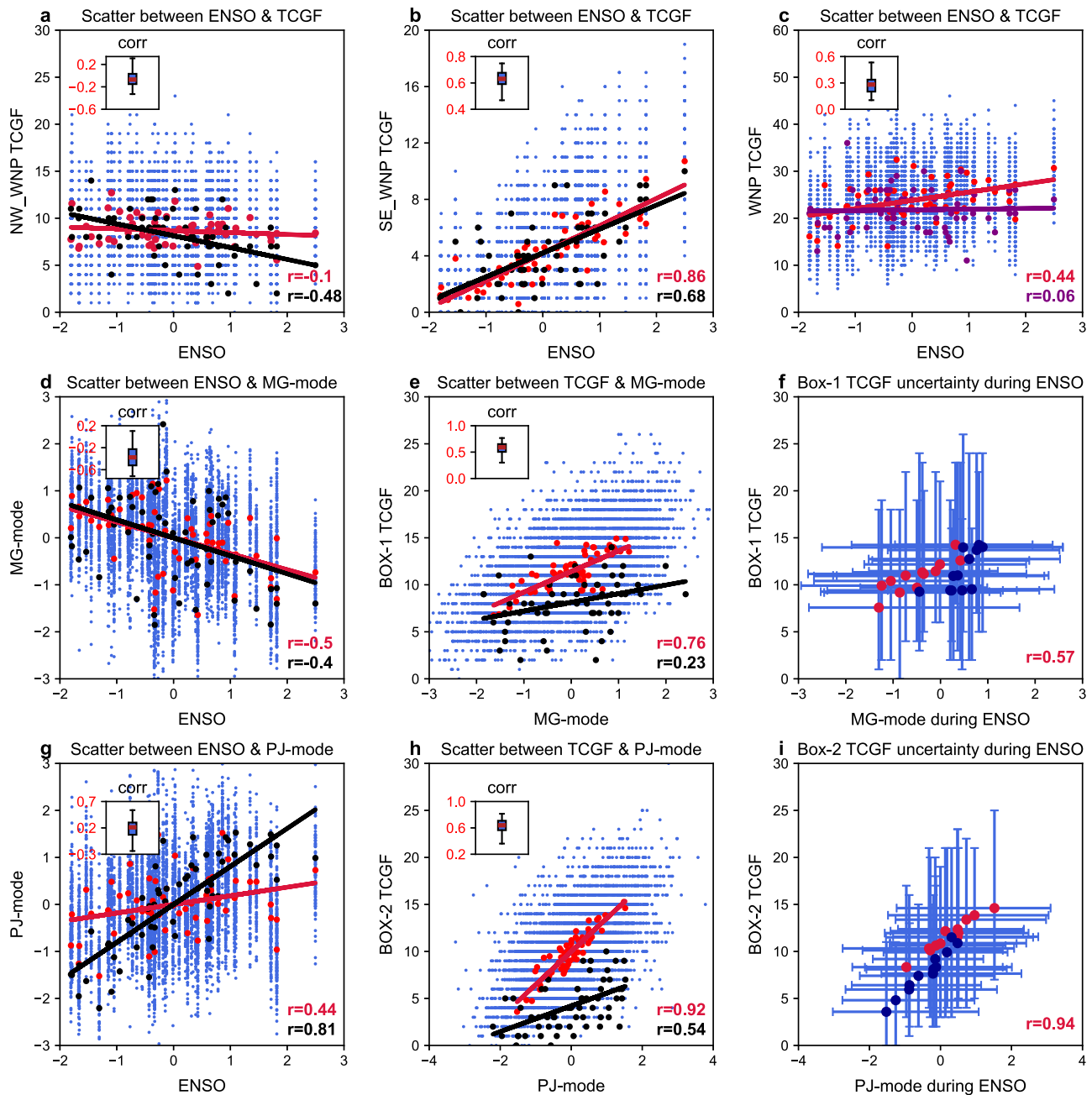
Fig. 3 Relationships among ENSO, the two atmospheric modes and TCGF. a–d Scatter plot between ENSO index and **a** TCGF over the NW_WNP, **b** TCGF over the SE_WNP, **c** WNP TCGF, and **d** the MG-mode; **e** scatter plot between the MG-mode and TCGF in Box-1 (Fig. 1h) for 100 members (red and blue) and observation (black); **f** the scatter plot between the ensemble mean of Box-1 TCGF and 24 ENSO events with the spreads of the MG-mode and Box-1 TCGF represented by the error bars; **g** scatter plot between ENSO and the PJ-mode with observation in black and simulations in red or blue; **h** scatter plot between the PJ-mode and TCGF in Box-2 (Fig. 1i) for 100 members; and **i** scatter plot between the ensemble mean of Box-2 TCGF and 24 ENSO events with the spreads of the PJ-mode and Box-2 TCGF represented by the error bars. The red and black dots in subplots except (**f, i**) indicate the ensemble mean of TCGF (MG-mode, PJ-mode and ENSO) in the MRI-AGCM model simulation and observation, respectively; and the regressed lines of the ensemble mean values are also shown in red and black. **f, i** The red dots represent the scatters between ensemble-averaged TCGF and El Niño events while the blue dots are the scatters between ensemble-averaged TCGF and La Niña events. The MG-mode is derived from the second mode of EOF analysis of 850-hPa winds in the region (Eq–35°N, 100°E–160°E) while the PJ-mode is obtained from the first mode of EOF analysis of 850-hPa vorticity in the region (10°N–55°N, 100°E–160°E) during 1951–2010. The correlation coefficients between two indices for the 100 members with the minimum, maximum, median, 25th and 75th percentile values are shown in each bar plot.

that the first two PCs of precipitation differences have significant correlations ($r = 0.64$ and 0.51) with those of the differences in the simulated TCGF (Fig. 6a, b). The regressed wind field with respective to PC1 shows a strong anomalous cyclonic circulation predominantly over the SCS and east of the Philippines, which plays a role in promoting local TC genesis (Fig. 6c), while the regressed wind field upon PC2 exhibits a basin-scale anomalous cyclonic circulation over the WNP (Fig. 6d). These two anomalous circulation patterns resemble the MG-mode and PJ-mode as identified earlier, and largely affect TCGF over the WNP and
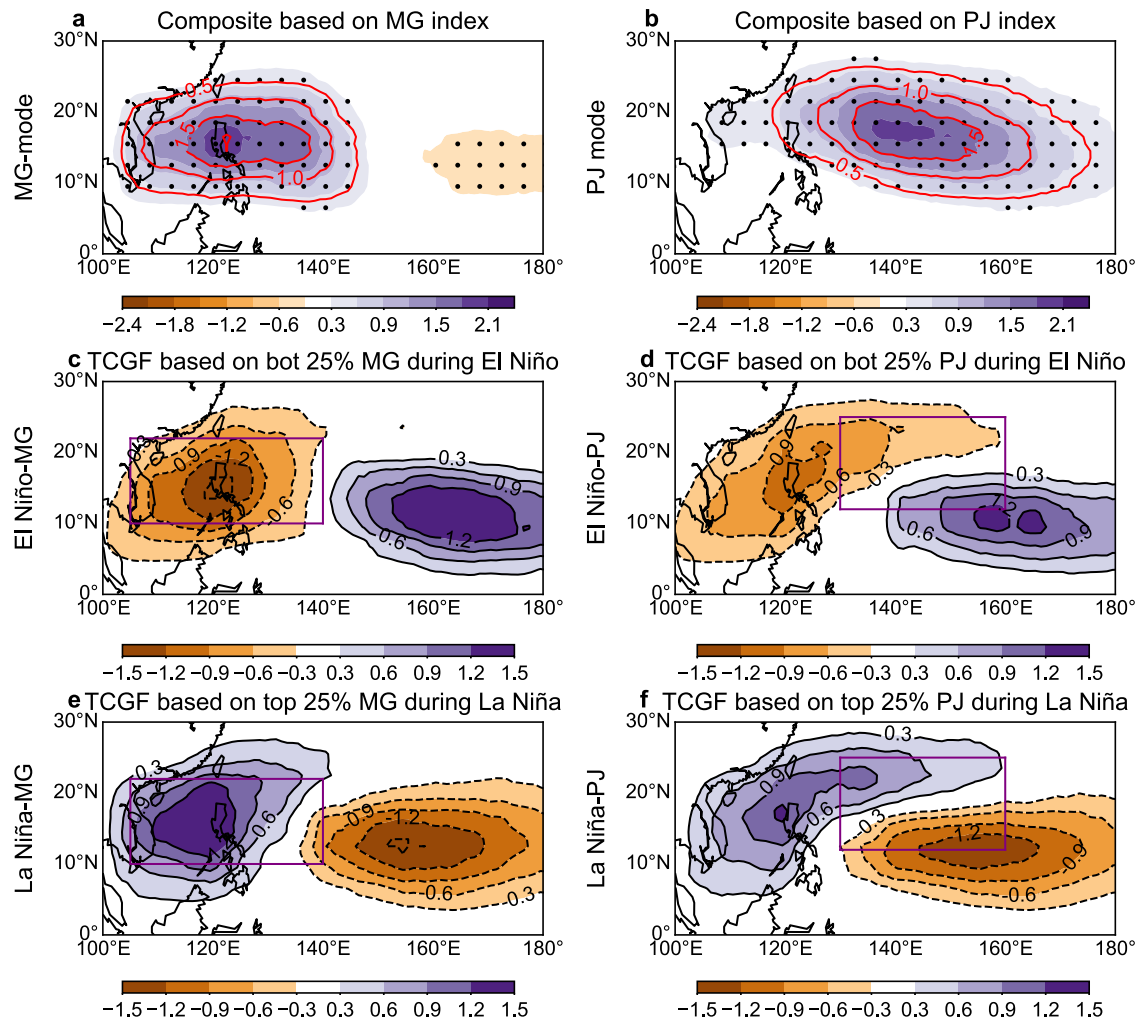
Fig. 4 Selected simulations of TCGF over the WNP in response to ENSO. a Composite difference in the simulated ensemble mean TCGF anomalies between positive and negative MG-mode events during 1951–2010 period; **b** as in (**a**) but between positive and negative PJ-mode events; **c**, **e** composite simulated TCGF anomalies (**c**) in El Niño years with a quarter of bottom (<=25%; anticyclonic anomaly) MG-mode values among the 100 ensemble members and **e** in La Niña events years with a quarter of top (>=25%; cyclonic anomaly) MG-mode values, respectively; **d**, **f** same as (**c**, **e**) but for PJ-mode (**d**) in El Niño years with the bottom 25th percentiles and **f** in La Niña years with the top 25th percentiles. The purple boxes in (**c**–**f**) represent the uncertainty regions of Box-1 and Box-2. Both the contours and the shading in (**a**, **b**) represent the composite difference in TCGF between positive and negative MG-mode (**a**) and PJ-mode (**b**) indices.

control the uncertainty in the simulated TCGF in Box-1 and Box-2 in response to ENSO (Fig. 1h, i).

To demonstrate how the precipitation-related diabatic heating anomaly triggers the two atmospheric modes mentioned above, we calculate the wave activity flux (WAF; Eq. (2) in Methods) related to the two EOF analyses of precipitation. The WAF related to the first EOF analysis propagates northward and westward, triggering the MG-mode over the western part of the WNP (Fig. 6e). The WAF related to the second EOF analysis of precipitation predominantly propagates northward, leading to the downstream development of the PJ-mode (Fig. 6f). We also examine the EOF analysis of JJASON precipitation by combining all 100-member data, namely 6000 model years (Supplementary Fig. 5). The two precipitation-induced atmospheric modes can be reproduced, consistent with those derived from the 100 members (Fig. 5). This means that the two atmospheric modes derived from precipitation data are dominant in all individual members. Therefore, the WAF analysis supports that anomalous diabatic heating associated with the simulated precipitation bias triggered the MG-mode and PJ-mode, which in turn contribute to the

uncertainty in the large-scale circulation that controls TCGF change over the WNP in response to ENSO.

DISCUSSION

Although the WNP TCGF difference between the warm and cold events shows a dipole pattern in observation, with positive and negative differences over the SE_WNP and NW_NWP, respectively, most state-of-the-art climate models can only capture the TCGF response to ENSO over the SE_WNP, with large uncertainty over the NW_NWP, as demonstrated using the 100 ensemble simulations in the MRI model. Further analyses show that the MG-mode and the PJ-mode largely modulate the simulated ENSO impacts on TCGF over the NW_WNP and thus are responsible for the uncertainty in the simulated TCGF therein. By constraining the two modes, we can significantly improve the TCGF simulations in response to ENSO. These two modes are shown to be triggered by the precipitation bias-related diabatic heating in the tropical western Pacific. A recent study[41] found that the simulation biases of Subtropical High and Monsoon could induce the simulated bias in TCGF. Although the Subtropical High is partially similar to the
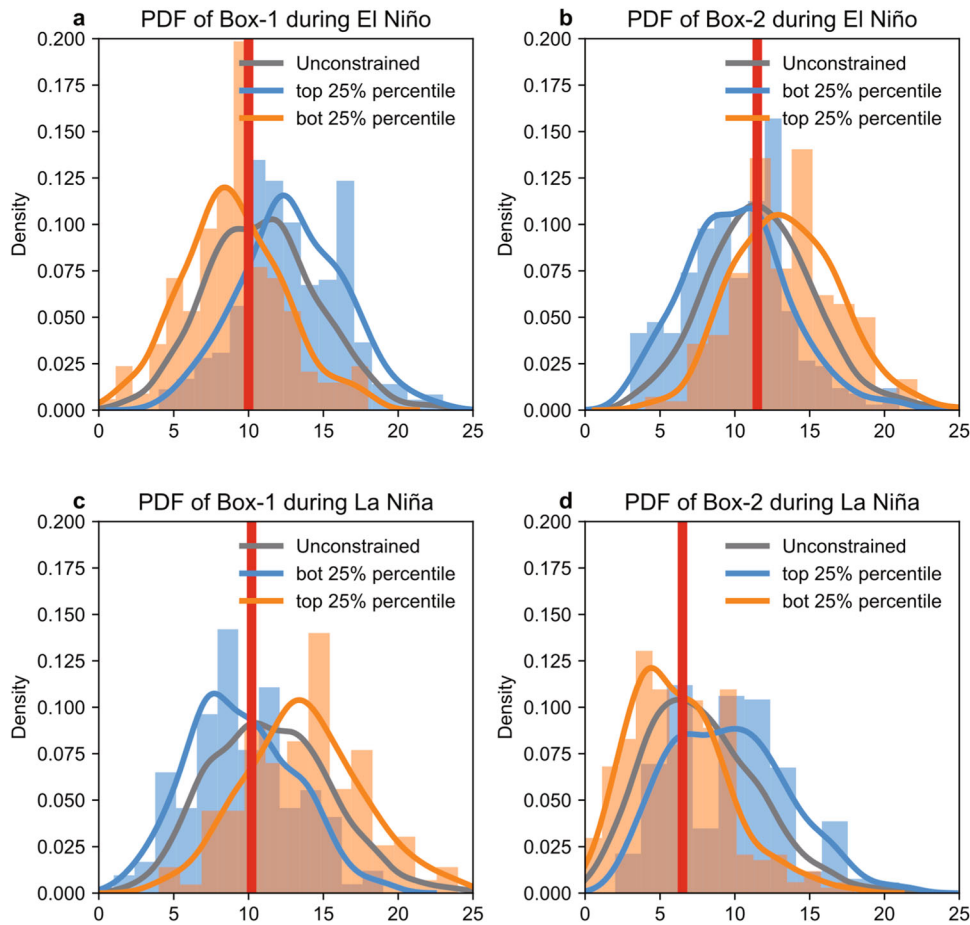
Fig. 5 Constrained simulations of WNP TCGF in response to ENSO. a Histogram (bar) and fitting distribution of unconstrained Box-1 TCGF (gray) and constrained (the bottom 25% percentile and the top 25% percentile of the sorted PC2 derived from EOF analysis of winds for 1951–2010) Box-1 TCGF in response to El Niño events; **b** histogram (bar) and fitting distribution of unconstrained Box-2 TCGF (gray) and constrained (the bottom 25% percentile and the top 25% percentile of the sorted PC1 derived from EOF analysis of winds for 1951–2010) Box-2 TCGF in response to El Niño events; **c** same as (**a**) but for La Niña events; and **d** same as (**b**) but for La Niña events. The red lines show the peak of PDF for unconstrained simulations.

two dynamical modes identified herein, they did not focus on the warm and cold ENSO phases. Furthermore, they emphasized the tropical-subtropical connections[41]. However, in this study, we revealed the simulation bias of diabatic heating in triggering "MG-mode" and "PJ-mode" and demonstrated the connection between diabatic heating associated with tropical precipitation and the atmospheric modes via the WAF mechanism.

Here, we only focused on the simulation uncertainty of TCGF related to the warm and cold ENSO phases. The simulation uncertainty of TCGF affected by other oceanic modes, such as the Pacific Meridional Mode[42–44], Eastern Indian Ocean and North Atlantic SST anomalies[45–48], is not touched upon in this study, which deserves a future investigation. Further, we only focused on the two atmospheric dynamical modes that contribute to the TCGF simulation uncertainty of TCGF associated with the two ENSO phases. However, the atmospheric modes could be very diverse over different basins, which warrants future studies. It is worthy of noting that the two atmospheric modes identified herein exist not only in the MRI atmospheric general circulation model (AGCM) but also in other models, including CESM, HadGEM, and ECMWF AGCM models. This indicates that the simulation uncertainty cannot be attributed to the variations in model physics[49–52], especially the convective parameterization scheme, which remains relatively independent in most climate models. Note that we did not consider the uncertainty induced by either the dynamical cores of the model nor contributed by the oceanic

internal or coupled variability in this study, which are more complicated. Since the 100-member atmospheric MRI model simulations were all forced by the same observed SST and sea ice content with only slight perturbation in the initial condition (see "Methods")[53,54], the diverse responses of the atmospheric circulations and TCGF to ENSO arise primarily from the internal variability in the model. A random perturbation, such as the precipitation bias in atmospheric models, could quickly grow[40] and self-aggregate[55] in numerical simulations, leading to significantly diverse atmospheric circulations.

Although many previous studies reported the systematic bias in the simulated precipitation in the warm pool region by state-of-the-art climate models, this study is the first to uncover that the precipitation bias-related atmospheric circulation anomaly (modes) can predominantly contribute to the uncertainty in the simulated TCGF over the NW_WNP in response to ENSO and thus the interannual variability of TC activity over the WNP. Our findings strongly suggest that to better simulate and predict TC activity over the WNP on interannual timescale, efforts should be made to improve the skill of climate models in simulating tropical precipitation, particularly in the western Pacific warm pool region. It is worthy of noting that the simulation uncertainty is not limited over the WNP, but widely spreaded over all TC basins on the globe. Therefore, the dynamical modes may vary in different basins. Last, we only derived two dynamical modes responsible for the simulation uncertainty of WNP TCGF in the present-day
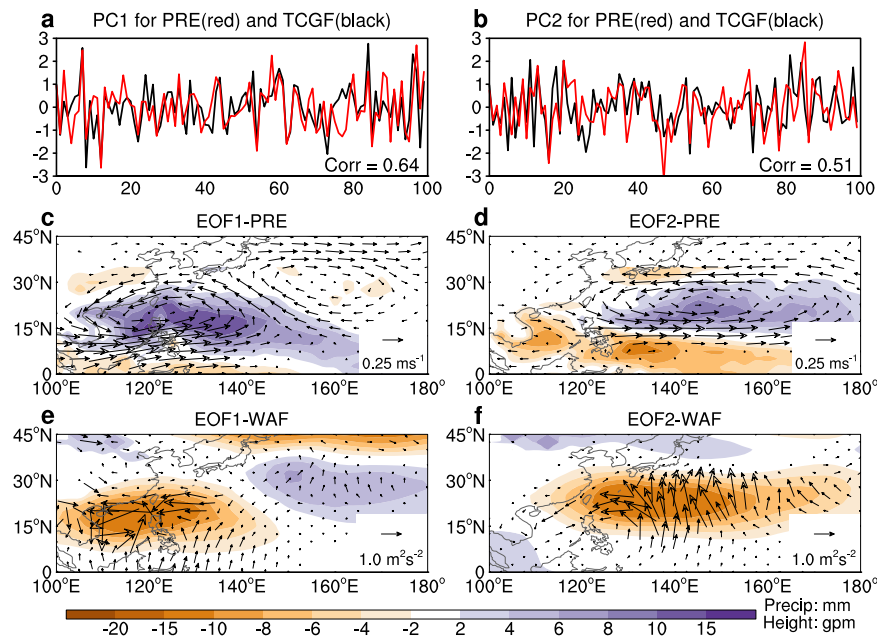
Fig. 6 The relationship between the precipitation biases and the two atmospheric modes. a The first principal component (PC1) of differences in the simulated precipitation (red) and TCGF (black) over the WNP between El Niño and La Niña events for 100 members; **b** as in (**a**) but for the second principal component (PC2); **c** the regressed winds at 850 hPa and precipitation upon PC1; **d** the regressed winds and precipitation upon PC2; **e** the WAF (unit: m² s⁻²) calculated based on the PC1-regressed streamfunction that is derived from the horizontal winds; **f** as in (**e**) but for the WAF related to PC2. The numbers in (**a**, **b**) represent the correlation coefficients between the two time series. The shades in (**c**, **d**) stand for differences in precipitation and in (**e**, **f**) for geopotential height (unit: gpm).

climate. These modes may be subject to change under anthropogenic forcing conditions, which deserves further investigations in the future.

METHODS

This section provides details of the data sources and methods used in this study. Various data sources from reanalysis and high-resolution model experiments were utilized to derive the TC information, validate the consistency of results, and examine the circulation patterns dominating the uncertainty of TCGF simulation in the WNP. Specifically, we conducted the EOF analysis of 100-member TCGF (850-hPa winds) differences between the warm and cold ENSO events to evaluate the uncertainty of TCGF (to obtain the internal atmospheric modes) over the WNP. In addition, we established the connection between the atmospheric modes and simulation uncertainty using correlation and regression analyses with Student's t test and bootstrap methods used for the significance test.

TC detection and tracking

The TC detection algorithm[11,14,16,31,56,57] was used to explicitly extract TC information from the fifth-generation European Center of Medium-Range Weather Forecasts (ECMWF) reanalysis (ERA5), HighResMIP models datasets of Coupled Model Intercomparison Project Phase 6 (CMIP6) and a database for Policy Decision marking for Future climate change (d4PDF). The basic extraction criteria and steps are as follows: First, there appears a low-pressure center on the sea surface. Considering that the TC intensity is initially weak, and the structure is asymmetric, the surface isobars is not necessary to be closed. Second, for the vortex to reach a TC strength, the 850-hPa wind speed was not less than $17\,m\,s^{-1}$ for the 0.5° HighResMIP models and ERA5 reanalysis, but for $13\,m\,s^{-1}$ for d4PDF data in its lifespan, and the absolute value of the 850-hPa vorticity was greater than $5 \times 10^{-5}\,s^{-1}$ ($8 \times 10^{-5}\,s^{-1}$ for MRI

model) at the same time. Third, the temperature within 1200 km from the vortex center was higher than the temperature between the radii of 1200 km–2400 km averaged between 300 and 500 hPa to ensure a warm core structure. Finally, the vortex lifespan should have been at least 1.5 days.

Reanalysis data

In this study, the monthly atmospheric data from 1951 to 2010, mainly including sea level pressure (SLP), 850-hPa and 200-hPa winds, were obtained from the National Centers for Environmental Prediction/National Centers for Atmospheric Research reanalysis I (NCEP/NCAR Reanalysis 1)[58] and from the ERA5[59] with the horizontal resolution of 0.25°. The vorticity and streamfunction are calculated from the 850-hPa horizontal winds, and the vertical zonal wind shear is calculated as the difference between 200- and 850-hPa zonal winds. We further used ERA5 reanalysis dataset, which has a horizontal resolution of 0.25° at 6-hourly interval, to derive the TC information, to cross-validate the observational TC data. The SST version 5 (SST v5) dataset was obtained from the National Oceanic and Atmospheric Administration (NOAA)[60]. The monthly precipitation dataset was got from Physical Sciences Laboratory (PSL) of NOAA.

Model data

This study mainly depended on the d4PDF dataset to quantify the uncertainty of TCGF simulation over the WNP and investigate the possible physical mechanisms. The atmospheric general circulation model version 3.2 (AGCM3.2) from the Meteorological Research Institute (MRI) of Japan has a horizontal resolution of about 60 km and 29 vertical levels, which can resolve the TC-like vortices. In particular, a cumulus convective scheme[50,61] was introduced in MRI-AGCM and it showed apparent improvements in simulating TCGF climatology. This model was driven by observational daily SST data from NOAA and daily sea ice content

data, while the anthropogenic forcing data were got from historical simulation of CMIP5, and the integration covers time periods during 1951–2010. A significant advance using the MRI-AGCM model is its 100-member ensemble simulations for d4PDF. The 100-member integrations were forced by the same observed SST and sea ice concentrations only with the initial atmospheric and lateral boundary conditions perturbed with a small magnitude[54,62]. The TC information, including longitudes, latitudes and intensities, was derived from the 6-hourly atmospheric data. We further used the monthly SLP, winds, geopotential height and precipitation data to analyze the circulation patterns responsible for the uncertainty of TCGF[63].

To check the dependence on model resolution, we employed a higher resolution of MRI-AGCM model with 20-km mesh to compare with the 60-km mesh simulation; the spatial correlation patterns simulated using the two resolutions (Fig. 1c–e) are similar over the NW_WNP with the correlations between observation and simulation being insignificant, indicating that the effect of model resolution is secondary. To address whether the uncertainty is partially originated from different model physics[31,49,64], we further used the TC data and monthly circulation data derived from the high-resolution ECMWF model (Fig. 1f), as well as other model datasets (Figure not shown)[11]. The results are consistent and indicate that the TC variability in response to ENSO contains large uncertainty over the NW_WNP. Note that only the high-resolution simulations from the MRI have enough ensemble members we can access for our EOF analysis, while other high-resolution datasets from various institutions either have no enough members or we could not access for reliable EOF analysis (Supplementary Table 1).

Observational TC dataset

Here, the TC dataset during 1951–2010 was downloaded from the International Best Track Archive for Climate Stewardship (IBTrACS)[65,66], which includes TC location (longitude and latitude) and intensity (maximum sustained surface wind speed) information at 6-hour interval. We considered a TC genesis as its intensity reached 35 knots (~17 ms^{-1}) for the first time over the WNP in IBTrACS data. The annual TCGF was summed from June to November (JJASON). Here, the study season from June to November basically covers the typhoon season (defined as June to October) and November, in which TCs are often largely modulated by ENSO, consistent with previous studies[67–69]. Note that we did not consider the seasonal dependence of simulation bias in this study[70,71], which could be a topic for a future study.

Definitions of TCGF, ENSO index, SNR, WAF, and two atmospheric modes

In this study, the TCGF at each grid was counted as the number of TCs that formed during JJASON in an area of 20° in the zonal direction and 10° in the meridional direction, centered at this grid box. The TCGF was calculated at a grid spacing of 1° so that a spatially smooth distribution can be ensured. Based on a previous study[11], this method could establish a stable relationship between the TCGF and the related environmental factors. The reason to set a 20°× 10° box is that the synoptic waves triggering TC genesis, such as equatorial Rossby waves, mixed-Rossby-gravity waves, and easterly waves, or other types of synoptic disturbances, have a zonal scale of about two thousand kilometers and a meridional e-folded scale of a thousand kilometer[72].

The Niño3.4 index was defined as the average SST over the equatorial eastern Pacific (5°S–5°N, 120°W–170°W). Here, we used JJASON averaged Niño3.4 index from PSL for the period of 1951–2010. The warm or cold ENSO events were defined using a 0.8 standard deviation (STD) threshold. From the 60-year dataset, we selected 12 El Niño (warm) events and 12 La Niña (cold) events. The 12 El Niño years are 1951, 1957, 1963, 1965, 1972, 1982, 1987,

1991, 1994, 1997, 2002, and 2009; the 12 La Niña cases are 1954, 1955, 1964, 1970, 1971, 1973, 1975, 1988, 1998, 1999, 2007 and 2010 as shown in Supplementary Fig. 6a. The composite of SST anomalies between positive and negative ENSO phases is shown in Supplementary Fig. 6b. The composite TCGF and circulations between the warm and cold ENSO events were defined as their response to ENSO. We also tested other thresholds, such as 1 STD and 0.6 °C, and even separated Central Pacific[73,74] from Canonical ENSO events. The results were similar.

The SNR in this study is defined as follow[49]:

$$SNR = \frac{\sigma_m}{\sigma_a} \qquad (1)$$

where σ_m is the STD of the randomly selected members from the ensemble mean, and σ_a is the STD of the departures from the ensemble mean in all 100 members or totally 6000 thousand years (60-year integration per member). In this study, the spreads of SNR (or correlations) were calculated by randomly selecting N ($N = 1, 5, 10, 20, 30, 40, 50, 60, 70, 80,$ and 90) members with 10,000 times repeated. After sorting 10,000 values, the values of minimum, maximum, median, 25th and 75th percentiles are shown in bar plots.

In this study, the empirical orthogonal function (EOF) analyses were conducted in two ways. First, based on the composite differences of TCGF (850-hPa winds) between the warm and cold ENSO events, we got 100 parallel samples of ENSO-related differences from the MRI-AGCM ensemble experiments. The deterministic or confidence of TCGF simulations can be determined by the similarities between ensemble members, while the uncertainty is originated from the differences between ensemble members. So, to quantify the uncertainty of TCGF and derive the atmospheric internal variability, we conducted EOF analysis of the 100-member composite differences of TCGF between the warm and cold ENSO events over the WNP (0–35°N, 100°E–180°). The spatial patterns indicate the regions containing the uncertainty in simulating the TCGF in response to ENSO using the MRI-AGCM. When we regressed 850-hPa winds upon the first and second principal components of EOF, we got the MG-type and PJ-type modes as discussed in the text (Fig. 2a, b). It is worthy of noting that, in this way, we consider the 100-member as the time dimension to derive the uncertainty mode among these 100 members[15], which is different from the method treating the real calendar year as the time dimension[71,75].

Although the MG-type and PJ-type modes can also be derived from the 850-hPa wind patterns for 100 ensemble members (Fig. 2a, b); it is still unknown whether the uncertainty of TCGF is induced by the fluctuations of these two atmospheric modes among members or they can be extracted from the annual JJASON wind data in each member. So, on the other hand, we further performed the traditional EOF analysis of JJASON winds and vorticity at 850 hPa during 1951–2010 for each member of the MRI-AGCM model by considering the real calendar year (1951–2010) as the time dimension. Basically, we conducted the EOF analysis for the composite differences in 850-hPa winds between the warm and cold ENSO events over the WNP (0–45°N, 100°E–180°). We found that the first EOF mode is very similar to the PJ-mode, and the second mode is similar to the MG-mode. We modified the EOF region to include higher latitudes (EQ–70°N, 100°E–160°E) and found that the correlations of the principal components between different domains are very high. To keep the integrity of the analysis, we considered the second EOF mode of 850-hPa wind differences over (0–35°N, 100°E–160°E) as the MG-mode (or Anticyclone mode) and treated the first EOF mode of 850-hPa vorticity over (10°N–55°N, 100°E–160°E) as the PJ-mode. We verified that the pattern correlations of MG or PJ-mode are very similar among members (Supplementary Fig. 3). By checking the first four EOF modes among the 100 members, we determined that most of the second (or first) EOF modes of 850-

hPa winds or vorticity are the MG (or PJ) mode. If the pattern correlation of winds between observation (Supplementary Fig. 3a or Fig. 3b) and the other three modes is higher than the second (or first) one, we considered the mode with highest pattern correlation as MG (or PJ) mode (Supplementary Fig. 3).

The wave activity flux (WAF) in the spherical coordinates can be expressed as follows[76]:

$$WAF = \frac{p\cos\phi}{2|\mathbf{U}|} \begin{pmatrix} \frac{U}{a^2\cos^2\phi}\left[\left(\frac{\partial\psi'}{\partial\lambda}\right)^2 - \psi'\frac{\partial^2\psi'}{\partial\lambda^2}\right] + \frac{V}{a^2\cos\phi}\left[\frac{\partial\psi'}{\partial\lambda}\frac{\partial\psi'}{\partial\phi} - \psi'\frac{\partial^2\psi'}{\partial\lambda\partial\phi}\right] \frac{U}{a^2\cos\phi}\left[\frac{\partial\psi'}{\partial\lambda}\frac{\partial\psi'}{\partial\phi} - \psi'\frac{\partial^2\psi'}{\partial\lambda\partial\phi}\right] + \frac{V}{a^2}\left[\left(\frac{\partial\psi'}{\partial\phi}\right)^2 - \psi'\frac{\partial^2\psi'}{\partial\phi^2}\right] \end{pmatrix}$$

(2)

Where U, V are the climatological zonal and meridional winds at 850 hPa for 100-member ensemble mean, respectively; ψ' is the regressed stream function (SF) anomaly upon respective principal components of EOF analysis; a, ϕ, and λ are the Earth's radius, latitude, and longitude; p is the air pressure at 1000-hPa. Instead of using a quasi-geostrophic approximation to derive the SF based on geopotential height, we derive the SF anomaly based on vorticity, which is further calculated from the zonal and meridional winds, by solving the differential equations $u' = \frac{1}{a}\frac{\partial\psi'}{\partial\phi}$ and $v' = -\frac{1}{a\cos\phi}\frac{\partial\psi'}{\partial\lambda}$.

Significance tests

Here, the statistical significance was detected based on the following methods: the two-tailed Student's t test for composite analysis, the two-sided bootstrap resampling test for spreads and the North test for EOF analysis. The degree of freedom of the Student's t test was 22 for composite analysis of the 24 ENSO events and 98 for the regressed analysis based on 100 members. The bootstrap test was used to evaluate the spreads of the correlations and SNR with 10,000 times resampling.

DATA AVAILABILITY

All datasets utilized in this study can be publicly accessed. The IBTrACS best-track dataset is available at https://www.ncdc.noaa.gov/ibtracs/; the 6-hourly and monthly reanalysis data of ERA5 and NCEP/NCAR reanalysis can be downloaded from https://www.ecmwf.int/en/forecasts/datasets/reanalysis-datasets/era5 and https://psl.noaa.gov/data/gridded/data.ncep.reanalysis.html, respectively; the d4PDF database of the MRI-AGCM for downloading 6-hourly and monthly datasets are available at http://d4pdf.diasjp.net/d4PDF.cgi?target=GCM-subset&lang=en; and the High-ResMIP data of the CMIP6 used to validate the d4PDF datasets are openly available at https://data.ceda.ac.uk/badc/cmip6/data/CMIP6/HighResMIP; the MRI 20-km TC dataset is provided by Prof. Yohei Yamada.

CODE AVAILABILITY

The Python codes used for plotting the figures in this study and Fortran codes for the TC detection in reanalysis and CMIP6-HighResMIP models can be requested from the first author and downloaded from the figshare website (https://doi.org/10.6084/m9.figshare.22756943.v1).

REFERENCES

1. Wu, L., Wang, C. & Wang, B. Westward shift of western North Pacific tropical cyclogenesis. *Geophys. Res. Lett.* **42**, 1537–1542 (2015).
2. Emanuel, K. Increasing destructiveness of tropical cyclones over the past 30 years. *Nature* **436**, 686–688 (2005).
3. Webster, P. J. Changes in tropical cyclone number, duration, and intensity in a warming environment. *Science* **309**, 1844–1846 (2005).
4. Jin, F.-F. An equatorial ocean recharge paradigm for ENSO. Part I: conceptual model. *J. Atmos. Sci.* **54**, 811–829 (1997).
5. Wang, B. & Chan, J. C. L. How strong ENSO events affect tropical storm activity over the Western North Pacific. *J. Clim.* **15**, 1643–1658 (2002).
6. Guo, Y.-P. & Tan, Z.-M. Westward migration of tropical cyclone rapid-intensification over the Northwestern Pacific during short duration El Niño. *Nat. Commun.* **9**, 1507 (2018).
7. Patricola, C. M., Chang, P. & Saravanan, R. Degree of simulated suppression of Atlantic tropical cyclones modulated by flavour of El Niño. *Nat. Geosci.* **9**, 155–160 (2016).
8. Camargo, S. J., Robertson, A. W., Gaffney, S. J., Smyth, P. & Ghil, M. Cluster analysis of typhoon tracks. Part II: large-scale circulation and ENSO. *J. Clim.* **20**, 3654–3676 (2007).
9. Hawkins, E. & Sutton, R. The potential to narrow uncertainty in regional climate predictions. *Bull. Am. Meteorol. Soc.* **90**, 1095–1108 (2009).
10. Zhou, T., Lu, J., Zhang, W. & Chen, Z. The sources of uncertainty in the projection of global land monsoon precipitation. *Geophys. Res. Lett.* **47**, e2020GL088415 (2020).
11. Song, K., Zhao, J., Zhan, R., Tao, L. & Chen, L. Confidence and uncertainty in simulating tropical cyclone long-term variability using the CMIP6-HighResMIP. *J. Clim.* **35**, 6431–6451 (2022).
12. Wu, M. et al. A very likely weakening of Pacific Walker Circulation in constrained near-future projections. *Nat. Commun.* **12**, 6502 (2021).
13. Murakami, H., Mizuta, R. & Shindo, E. Future changes in tropical cyclone activity projected by multi-physics and multi-SST ensemble experiments using the 60-km-mesh MRI-AGCM. *Clim. Dyn.* **39**, 2569–2584 (2012).
14. Zhao, J., Zhan, R., Wang, Y., Xie, S.-P. & Wu, Q. Untangling impacts of global warming and Interdecadal Pacific Oscillation on long-term variability of North Pacific tropical cyclone track density. *Sci. Adv.* **6**, eaba6813 (2020).
15. Huang, X. et al. South Asian summer monsoon projections constrained by the interdecadal Pacific oscillation. *Sci. Adv.* **6**, eaay6546 (2020).
16. Zhao, J., Zhan, R. & Wang, Y. Different responses of tropical cyclone tracks over the western North Pacific and North Atlantic to two distinct SST warming patterns. *Geophys. Res. Lett.* **47**, e2019GL086923 (2020).
17. Cao, J., Zhao, H., Wang, B. & Wu, L. Hemisphere-asymmetric tropical cyclones response to anthropogenic aerosol forcing. *Nat. Commun.* **12**, 6787 (2021).
18. Dong, L. & Leung, L. R. Winter precipitation changes in California under global warming: contributions of CO_2, uniform SST warming, and SST change patterns. *Geophys. Res. Lett.* **48**, e2020GL091736 (2021).
19. Dong, L., Leung, L. R., Song, F. & Lu, J. Uncertainty in El Niño-like warming and California precipitation changes linked by the Interdecadal Pacific Oscillation. *Nat. Commun.* **12**, 6484 (2021).
20. Seager, R. et al. Strengthening tropical Pacific zonal sea surface temperature gradient consistent with rising greenhouse gases. *Nat. Clim. Change* **9**, 517–522 (2019).
21. Xie, S. Ocean warming pattern effect on global and regional climate change. *AGU Adv.* **1**, e2019AV000130 (2020).
22. Murakami, H. et al. Detected climatic change in global distribution of tropical cyclones. *Proc. Natl. Acad. Sci. USA* **117**, 10706–10714 (2020).
23. Meehl, G. A., Hu, A., Santer, B. D. & Xie, S.-P. Contribution of the Interdecadal Pacific Oscillation to twentieth-century global surface temperature trends. *Nat. Clim. Change* **6**, 1005–1008 (2016).
24. Zhao, J., Zhan, R., Wang, Y. & Xu, H. Contribution of Interdecadal Pacific Oscillation to the recent abrupt decrease in tropical cyclone genesis frequency over the western North Pacific since 1998. *J. Clim.* **31**, 8211–8224 (2018).
25. Zhang, W. et al. Dominant role of Atlantic Multidecadal Oscillation in the recent decadal changes in Western North Pacific tropical cyclone activity. *Geophys. Res. Lett.* **45**, e2017GL076397 (2018).
26. Wang, C., Wang, B., Wu, L. & Luo, J.-J. A see-saw variability in tropical cyclone genesis between the western North Pacific and the North Atlantic shaped by Atlantic multidecadal variability. *J. Clim.* **35**, 2479–2489 (2022).
27. Chan, J. C. L. Tropical cyclone activity in the Northwest Pacific in relation to the El Niño/Southern Oscillation phenomenon. *Mon. Weather Rev.* **113**, 599–606 (1985).
28. Chan, J. C. L. Tropical cyclone activity over the Western North Pacific associated with El Niño and La Niña Events. *J. Clim.* **13**, 2960–2972 (2000).
29. Camargo, S. J. & Sobel, A. H. Western North Pacific tropical cyclone intensity and ENSO. *J. Clim.* **18**, 2996–3006 (2005).
30. Roberts, M. J. et al. Impact of model resolution on tropical cyclone simulation using the HighResMIP–PRIMAVERA multimodel ensemble. *J. Clim.* **33**, 2557–2583 (2020).
31. Murakami, H., Wang, B. & Kitoh, A. Future change of western North Pacific typhoons: projections by a 20-km-mesh global atmospheric model. *J. Clim.* **24**, 1154–1169 (2011).
32. North, G. R., Bell, T. L., Cahalan, R. F. & Moeng, F. J. Sampling errors in the estimation of empirical orthogonal functions. *Mon. Weather Rev.* **110**, 699–706 (1982).
33. Gill, A. E. Some simple solutions for heat-induced tropical circulation. *Q. J. R. Meteorol. Soc.* **106**, 447–462 (1980).

34. Matsuno, T. Quasi-geostrophic motions in the equatorial area. *J. Meteorol. Soc. Jpn. Ser. II* **44**, 25–43 (1966).

35. Nitta, T. Global features of the Pacific-Japan oscillation. *Meteorol. Atmos. Phys.* **41**, 5–12 (1989).

36. Tao, L., Li, T., Ke, Y.-H. & Zhao, J.-W. Causes of interannual and interdecadal variations of the summertime Pacific-Japan-like pattern over East Asia. *J. Clim.* **30**, 8845–8864 (2017).

37. Ronghui, H. & Li, L. Numerical simulation of the relationship between the anomaly of subtropical high over East Asia and the convective activities in the western tropical Pacific. *Adv. Atmos. Sci.* **6**, 202–214 (1989).

38. Kubota, H., Kosaka, Y. & Xie, S. A 117-year long index of the Pacific-Japan pattern with application to interdecadal variability. *Int. J. Climatol.* **36**, 1575–1589 (2016).

39. Chen, G. & Tam, C.-Y. Different impacts of two kinds of Pacific Ocean warming on tropical cyclone frequency over the western North Pacific. *Geophys. Res. Lett.* **37**, L0803 (2010).

40. Cai, W. et al. Butterfly effect and a self-modulating El Niño response to global warming. *Nature* **585**, 68–73 (2020).

41. Feng, X., Toumi, R., Roberts, M., Hodges, K. I. & Vidale, P. L. An approach to link climate model tropical cyclogenesis bias to large-scale wind circulation modes. *Geophys. Res. Lett.* **50**, e2023GL103838 (2023).

42. Zhang, W., Vecchi, G. A., Murakami, H., Villarini, G. & Jia, L. The Pacific Meridional Mode and the occurrence of tropical cyclones in the western North Pacific. *J. Clim.* **29**, 381–398 (2016).

43. Liu, C., Zhang, W., Stuecker, M. F. & Jin, F. Pacific Meridional Mode-Western North Pacific tropical cyclone linkage explained by tropical Pacific quasi-decadal variability. *Geophys. Res. Lett.* **46**, 13346–13354 (2019).

44. Wu, Q., Zhao, J., Zhan, R. & Gao, J. Revisiting the interannual impact of the Pacific Meridional Mode on tropical cyclone genesis frequency in the Western North Pacific. *Clim. Dyn.* **56**, 1003–1015 (2021).

45. Zhan, R., Wang, Y. & Wu, C.-C. Impact of SSTA in the East Indian Ocean on the frequency of Northwest Pacific tropical cyclones: a regional atmospheric model study. *J. Clim.* **24**, 6227–6242 (2011).

46. Zhan, R., Wang, Y. & Lei, X. Contributions of ENSO and East Indian Ocean SSTA to the interannual variability of Northwest Pacific tropical cyclone frequency. *J. Clim.* **24**, 509–521 (2011).

47. Ham, Y.-G., Kug, J.-S., Park, J.-Y. & Jin, F.-F. Sea surface temperature in the north tropical Atlantic as a trigger for El Niño/Southern Oscillation events. *Nat. Geosci.* **6**, 112–116 (2013).

48. Yu, J., Li, T., Tan, Z. & Zhu, Z. Effects of tropical North Atlantic SST on tropical cyclone genesis in the western North Pacific. *Clim. Dyn.* **46**, 865–877 (2016).

49. Mei, W., Kamae, Y., Xie, S.-P. & Yoshida, K. Variability and predictability of North Atlantic hurricane frequency in a large ensemble of high-resolution atmospheric simulations. *J. Clim.* **32**, 3153–3167 (2019).

50. Tiedtke, M. A comprehensive mass flux scheme for cumulus parameterization in large-scale models. *Mon. Weather Rev.* **117**, 1779–1800 (1989).

51. Zhang, G. J. & McFarlane, N. A. Sensitivity of climate simulations to the parameterization of cumulus convection in the Canadian climate centre general circulation model. *Atmos Ocean* **33**, 407–446 (1995).

52. Nordeng, T. E. Extended versions of the convective parameterization scheme at ECMWF and their impact on the mean and transient activity of the model in the tropics. *ECMWF Res. Dep. Tech Memo* **206**, 1–41 (1994).

53. Roberts, M. J. et al. Projected future changes in tropical cyclones using the CMIP6 HighResMIP multimodel ensemble. *Geophys. Res. Lett.* **47**, e2020GL088662 (2020).

54. Mizuta, R. et al. Over 5000 years of ensemble future climate simulations by 60-km global and 20-km regional atmospheric models. *Bull. Am. Meteorol. Soc.* **98**, 1383–1398 (2017).

55. Wing, A. A., Emanuel, K., Holloway, C. E. & Muller, C. Convective self-aggregation in numerical simulations: a review. *Surv. Geophys.* **38**, 1173–1197 (2017).

56. Zhao, M., Held, I. M., Lin, S.-J. & Vecchi, G. A. Simulations of global hurricane climatology, interannual variability, and response to global warming using a 50-km resolution GCM. *J. Clim.* **22**, 6653–6678 (2009).

57. Murakami, H. et al. Future changes in tropical cyclone activity projected by the new high-resolution MRI-AGCM. *J. Clim.* **25**, 3237–3260 (2012).

58. Kalnay, E. et al. The NCEP/NCAR 40-year reanalysis project. *Bull. Am. Meteorol. Soc.* **77**, 437–471 (1996).

59. Hersbach, H. et al. The ERA5 global reanalysis. *Q. J. R. Meteorol. Soc.* **146**, 1999–2049 (2020).

60. Huang, B. et al. Extended reconstructed sea surface temperature, Version 5 (ERSSTv5): upgrades, validations, and intercomparisons. *J. Clim.* **30**, 8179–8205 (2017).

61. Yoshimura, H., Mizuta, R. & Murakami, H. A spectral cumulus parameterization scheme interpolating between two convective updrafts with semi-Lagrangian calculation of transport by compensatory subsidence. *Mon. Weather Rev.* **143**, 597–621 (2015).

62. Ishii, M. & Mori, N. d4PDF: large-ensemble and high-resolution climate simulations for global warming risk assessment. *Prog. Earth Planet. Sci.* **7**, 58 (2020).

63. Yoshida, K., Sugi, M., Mizuta, R., Murakami, H. & Ishii, M. Future changes in tropical cyclone activity in high-resolution large-ensemble simulations. *Geophys. Res. Lett.* **44**, 9910–9917 (2017).

64. Yokoi, S., Takayabu, Y. N. & Chan, J. C. L. Tropical cyclone genesis frequency over the western North Pacific simulated in medium-resolution coupled general circulation models. *Clim. Dyn.* **33**, 665–683 (2009).

65. Knapp, K. R., Kruk, M. C., Levinson, D. H., Diamond, H. J. & Neumann, C. J. The International Best Track Archive for Climate Stewardship (IBTrACS): unifying tropical cyclone data. *Bull. Am. Meteorol. Soc.* **91**, 363–376 (2010).

66. Schreck, C. J., Knapp, K. R. & Kossin, J. P. The impact of best track discrepancies on global tropical cyclone climatologies using IBTrACS. *Mon. Weather Rev.* **142**, 3881–3899 (2014).

67. Mei, W. & Li, S. Variability and predictability of basinwide and sub-basin tropical cyclone genesis frequency in the Northwest Pacific. *J. Clim.* **35**, 3265–3284 (2022).

68. Li, S., Mei, W. & Xie, S.-P. Effects of tropical sea surface temperature variability on Northern Hemisphere tropical cyclone genesis. *J. Clim.* **35**, 4719–4739 (2022).

69. Zhao, J., Zhan, R., Wang, Y., Jiang, L. & Huang, X. A multiscale-model-based near-term prediction of tropical cyclone genesis frequency in the Northern Hemisphere. *J. Geophys. Res. Atmos.* **127**, e2022JD037267 (2022).

70. Basconcillo, J. & Moon, I.-J. Increasing activity of tropical cyclones in East Asia during the mature boreal autumn linked to long-term climate variability. *NPJ Clim. Atmos. Sci.* **5**, 4 (2022).

71. Zhang, D. & Chen, L. Hybrid statistical–dynamical seasonal prediction of tropical cyclone track density over Western North Pacific. *Clim. Dyn.* **60**, 2517–2532 (2023).

72. Chen, G. & Chou, C. Joint Contribution of multiple equatorial waves to tropical cyclogenesis over the Western North Pacific. *Mon. Weather Rev.* **142**, 79–93 (2014).

73. Ashok, K. & Yamagata, T. Climate change: the El Niño with a difference. *Nature* **461**, 481–484 (2009).

74. Kug, J.-S., Jin, F.-F. & An, S.-I. Two types of El Niño events: cold tongue El Niño and Warm Pool El Niño. *J. Clim.* **22**, 1499–1515 (2009).

75. Yu, H., Wang, C. & Ge, X. Modulation of Pacific sea surface temperatures on the late-season tropical cyclone tracks over the western North Pacific and its implication for seasonal forecasting. *Front Earth Sci.* **10**, 835001 (2022).

76. Takaya, K. & Nakaruma, H. A formulation of a phase-independent wave-activity flux of stationary and migratory quasi-geostrophic eddies on a zonally varying basic flow. *J. Atmos. Sci.* **58**, 608–627 (2001).

ACKNOWLEDGEMENTS

AUTHOR CONTRIBUTIONS

J.Z., R.Z., H.M. and Y.W. conceived main parts of this study and draft the initial manuscript. J.Z. and L.Z. conducted the data analyses. S.P. and Y.G. contributed to the improvement of the manuscript. All authors read and approved the manuscript.

COMPETING INTERESTS

The authors declare no competing interests.

ADDITIONAL INFORMATION

Supplementary information The online version contains supplementary material available at https://doi.org/10.1038/s41612-023-00537-6.

Correspondence and requests for materials should be addressed to Ruifen Zhan or Yuqing Wang.

Reprints and permission information is available at http://www.nature.com/reprints

Publisher's note Springer Nature remains neutral with regard to jurisdictional claims in published maps and institutional affiliations.